Research Square

Preprints are preliminary reports that have not undergone peer review.
They should not be considered conclusive, used to inform clinical practice,
or referenced by the media as validated information.

A Parameterized Data-Driven Neural Network with Physics-Based Regularization for Thermal Field Prediction in Metal Additive Manufacturing

Aishwarya Manjunath
University of North Texas
Hang Tran
University of North Texas
Selvamurugan Palaniappan
University of North Texas
Shashank Sharma
University of North Texas
Song Fu
University of North Texas
Narendra B. Dahotre
narendra.dahotre@unt.edu

University of North Texas https://orcid.org/0000-0003-2302-9028

Research Article

Keywords: Physics-based regularization, Thermal profiles, Additive manufacturing, Finite Element Method, Deep learning, Physics Informed Machine Learning

Posted Date: July 24th, 2026

DOI: https://doi.org/10.21203/rs.3.rs-10362204/v1

License: This work is licensed under a Creative Commons Attribution 4.0 International License.
Read Full License

A Parameterized Data-Driven Neural Network with Physics-Based Regularization for Thermal Field Prediction in Metal Additive Manufacturing

Aishwarya Manjunath[1,2], Hang Tran[1,2], Selvamurugan Palaniappan[1,3], Shashank Sharma[1,3], Song Fu[2], Narendra B. Dahotre[1,3*]

[1*]Center for Agile and Adaptive Additive Manufacturing (CAAAM), University of North Texas, Denton, TX, 76207, USA.
[2]Department of Computer Science, University of North Texas, Denton, TX, 76207, USA.
[3]Department of Material Science and Engineering, University of North Texas, Denton, TX, 76207, USA.

*Corresponding author(s). E-mail(s): narendra.dahotre@unt.edu;
Contributing authors: aishwaryamanjunath@my.unt.edu; hangtran3@my.unt.edu; SelvamuruganP@my.unt.edu; shashank.sharma@unt.edu; song.fu@unt.edu;

Abstract

Laser Powder Bed Fusion (L-PBF) is a metal additive manufacturing process characterized by highly transient and localized thermal behavior that strongly influences melt pool evolution and the resulting material properties. Accurate prediction of the spatiotemporal temperature field is therefore essential for process optimization, but conventional numerical simulations remain computationally expensive for large parametric studies. In this work, a parameterized data-driven neural network with physics-based regularization is developed for predicting transient thermal fields in SS316L across varying laser power and scan speed conditions. The framework incorporates process parameters directly into the input space together with spatiotemporal coordinates, enabling continuous thermal prediction within the bounded process domain. High-fidelity finite element method (FEM) thermal simulations provide the primary supervision, while the transient heat conduction equation is incorporated as a physics-based regularization term during training. The proposed framework achieves an RMSE of 9.01 K while accurately predicting thermal fields and melt pool geometry.

Keywords: Physics-based regularization, Thermal profiles, Additive manufacturing, Finite Element Method, Deep learning, Physics Informed Machine Learning.

1 Introduction

Metal additive manufacturing (AM) techniques, such as Laser Powder Bed Fusion (L-PBF), have emerged as advanced manufacturing paradigms capable of fabricating geometrically complex, high-density components with reduced material waste and shorter production cycles [1, 2]. In this technique, a focused laser selectively melts metallic powder in a layer-wise manner, resulting in highly localized and transient thermal gradients governed by laser–material interaction, heat transfer, and phase transformation phenomena [3].

As a consequence, these AM processes are characterized by complex thermal fields that directly govern melt pool dynamics, residual stress evolution, and the resulting microstructural properties of fabricated components [4, 5]. The spatiotemporal thermal profile generated during L-PBF plays a critical role in determining melt pool geometry and solidification behavior, which in turn influence the mechanical performance of fabricated parts [6]. This close relationship between thermal behavior and material properties highlights the need for accurate thermal prediction for process optimization, defect reduction, and digital twin development [7–10].

Physics-based numerical approaches, including finite element methods (FEM), computational fluid dynamics (CFD), and lattice Boltzmann methods (LBM), have been extensively used to model thermal behavior in AM processes [11, 12]. While these models provide physically interpretable and high-fidelity predictions, their computational cost limits their applicability for real-time prediction, parametric studies, and large-scale process optimization [13]. This computational limitation has motivated the exploration of alternative surrogate machine learning approaches [4, 14].

Data-driven machine learning (ML) models have been explored as computationally efficient surrogates for thermal prediction. Early approaches, including tree-based models, multilayer perceptrons (MLPs), and convolutional neural networks (CNNs), demonstrated significant improvements in inference speed and predictive capability for melt pool characteristics and temperature evolution [3, 15, 16]. However, these models often require large training datasets, lack physical interpretability, and exhibit limited robustness across varying process conditions [3, 15, 16]. Furthermore, adapting such models to new materials or process parameters typically requires retraining or redesign, limiting their scalability. Beyond regression-based models, generative approaches have also been explored to capture high-dimensional thermal fields and complex spatial patterns. In particular, Generative Adversarial Networks (GANs) have shown promise in synthesizing thermal distributions and microstructural features by learning underlying data distributions [17–21]. However, their applicability to physics informed thermal prediction remains limited.

Therefore, Physics-informed machine learning (PIML) approaches were subsequently introduced to incorporate governing physical laws directly into the learning process [22]. In particular, Physics-Informed Neural Networks (PINNs) embed heat transfer partial differential equations into the network loss function, enabling physically consistent predictions while reducing dependence on large datasets [4, 11, 23]. Recent studies have also explored parametric PINN formulations for thermal analysis in LPBF, where the heat equation is solved across varying material properties and process parameters [24]. While such approaches demonstrate the capability of PINNs to provide rapid parametric solutions with minimal computational cost, they often rely on simplified physics assumptions and predefined heat source formulations, limiting their applicability to complex, data-rich manufacturing scenarios. As mesh-free solvers, PINNs also eliminate the need for explicit mesh generation, offering improved flexibility over traditional numerical methods [4].

More recently, operator learning methods have been introduced to model mappings between functional spaces rather than discrete data points [25]. While such approaches demonstrate strong generalization capabilities, they typically rely on large volumes of high-fidelity simulation data for effective training, making them less data-efficient in scenarios where data generation is computationally expensive.

Despite these advancements, a critical limitation persists across existing frameworks: most models fail to inherently generalize across unseen process parameter combinations. Conventional PINN formulations are typically restricted to fixed boundary conditions and machine settings, requiring retraining or transfer learning when key parameters, such as laser power or scanning speed, are modified [26, 27]. This limitation restricts rapid, on-the-fly decision-making and limits the practical deployment of such models in process optimization and digital twin applications.

To systematically compare existing approaches and highlight this gap, Table 1 presents a detailed technical analysis of current methodologies, focusing on their inputs, generalization capabilities, and limitations.

Table 1: Comparative analysis of machine learning and physics-informed approaches for parametric thermal profile prediction in additive manufacturing.

Method	Model Type	Conditioning / Inputs	Generalization Capability / Prediction Scope	Key Limitations
Standard & Thermoelastic PINNs [14, 26, 27]	Physics-informed neural network (PINN)	Spatiotemporal coordinates (x, y, z, t)	Limited; predicts temperature fields for fixed parameter settings and requires retraining for new conditions	Excludes complex melt pool physics; inefficient for high-dimensional parameter exploration
Parametric PINNs (Single-track LPBF) [24]	Unsupervised physics-informed neural network	(x, y, z, t) + process/material parameters (e.g., P, v, k, C_p)	Moderate; predicts temperature fields and melt-pool dimensions across parameter ranges in a simplified single-track domain	Relies on predefined analytical heat-source models; assumes simplified continuum physics; excludes molten-metal flow and defect mechanisms; limited to single-track cases
Parameterized PINNs (Multi-Parameter) [5, 28, 29]	Parameterized PINN	(x, y, z, t) + process parameters (P, v, h)	Moderate; predicts temperature fields and melt-pool characteristics within the trained parameter range	High computational cost with increasing parameter dimensionality; scalability challenges for 3D multi-physics problems
Physics-Informed ConvLSTM [30]	Physics-informed sequence model	Sequential thermal images + physics-based heat-flux inputs	Limited; predicts future temperature fields from prior thermal history but requires observations for new conditions	Requires in-situ sensing; restricted to 2D prediction; simplified physics can produce residual errors
Physics-Informed CAE [31]	Physics-informed convolutional autoencoder	Temperature fields, geometry, heat flux	Moderate; predicts temperature fields while generalizing across geometries and toolpaths	Limited physical representation; does not directly map process parameters to thermal outcomes
Path-Aware PINNs [32]	PINN with path-aware constraints	(x, y, z, t) + laser path variables	Moderate; predicts temperature distributions and thermal anomalies across toolpaths and multi-laser configurations	Simplified physics; limited treatment of coupled thermomechanical interactions
Fourier Neural Operator (FNO) [25]	Operator learning model	Process parameters / functional inputs	Strong; predicts full spatiotemporal temperature fields across unseen parameter combinations within the learned distribution	Data-intensive; relies on large high-fidelity simulation datasets; limited physical interpretability

To address the limitations of existing approaches, this study presents a parameterized data-driven neural network framework with physics-based regularization for thermal field prediction in metal additive manufacturing. The framework is trained through supervised learning using high-fidelity FEM-generated thermal data, while the governing transient heat conduction equation is incorporated as a physics-based regularization term during optimization. Balanced sampling of critical thermal regions, consistent normalization across parameter combinations, and a staged training strategy are incorporated to facilitate learning across the highly non-uniform thermal domain encountered in L-PBF.

This hybrid formulation enables generalization across previously unseen combinations of process parameters within a single trained model for SS316L while maintaining accurate predictions across both localized melt pool regions and the broader thermal field. The resulting framework provides a scalable, data-efficient, and physically consistent surrogate for parametric thermal modeling and supports practical deployment in process optimization and digital twin applications.

2 Dataset

2.1 Data Generation

2.1.1 Numerical Model

The present study employed a 3D FEM-based heat transfer model to generate single-track thermal profiles during L-PBF-based AM. As reported in the literature, laser-matter interaction involves complex phenomena such as multiple reflections of the laser beam, highly dynamic melt pool convection, and vaporization-induced melt pool oscillations [33]. The dynamic coupling of laser absorption and melt pool oscillation results in different modes of melting (conduction, transition, and keyhole) with variations in process parameters (laser power, scanning velocity, hatch spacing, and layer thickness) [34, 35]. In light of these considerations, incorporating the aforementioned physical aspects into the numerical model is essential for accurately representing thermal profiles in the L-PBF process. However, the inclusion of such complex phenomena inevitably leads to increased computational run-time, which can hinder the generation of the extensive datasets required for ML algorithms [33, 34, 36]. Therefore, to efficiently generate a sufficient dataset for the proposed data-driven framework, a computationally tractable approach was adopted. In this approach, the laser-matter interaction and melt pool convection were compensated by an experimentally derived volumetric heat source [37, 38]. Primarily, as a proof of concept, thermal profiles on a single layer were generated and utilized to train the proposed data-driven neural network framework. It is important to note that this framework is not limited to single-layer predictions; the numerical model and the resulting machine learning predictions can be seamlessly extended to accommodate multi-track, multi-layer thermal profile predictions. Parametric variations in machine settings and material properties were employed to produce the thermal profile data. The mathematical formulation and the modeling framework are described in the following subsections.

2.1.2 3D Transient Thermal Model

The governing equation related to the heat transfer model is expressed as the following equation [33, 34]:

$$\rho C_p \frac{\partial T}{\partial t} = \nabla \cdot (k \nabla T) + q''' \tag{1}$$

In the above equation, the delineation between the powder bed and the melt pool was employed using the effective thermal properties of the powder bed, accounting for the inter-particle porosity. The effective density of the powder bed (ρ_p) can be expressed as [39].

$$\rho_p = \begin{cases} (1-\phi)\rho, & T < T_m \\ \rho, & T > T_m \end{cases} \tag{2}$$

A similar expression can be used for specific heat C_p. The effective thermal conductivity (k_p) of the powder bed was modeled as a function of the bulk thermal conductivity (k), the thermal conductivity of the surrounding gas or air (k_a), the powder packing density (ϕ), and the radiative effects within the powder bed (k_r). This relationship is captured in the following Eq. 3 [40]:

$$\frac{k_p}{k_a} = \left(1 - \sqrt{1-\phi}\right)\left(1 + \phi\frac{k_r}{k_a}\right) + \sqrt{1-\phi}\left[\frac{2}{1-\frac{k_a}{k}}\left(\frac{k}{k_a}\ln\left(\frac{k}{k_a}\right) - 1\right) + \frac{k_r}{k_a}\right] \tag{3}$$

The laser-irradiated surface of the computational domain was prescribed with the following conditions:

$$-k\frac{\partial T}{\partial z} = -h_c\left[T - T_{\text{amb}}\right] - \epsilon\sigma_b\left[T^4 - T_{\text{amb}}^4\right] \tag{4}$$

The non-irradiated boundary surfaces were prescribed with the following boundary condition:

$$-k\frac{\partial T}{\partial n} = -h_c\left[T - T_{\text{amb}}\right] \tag{5}$$

The vaporization heat flux, which accounts for heat loss due to material vaporization, can be expressed as:

$$q_{\text{evap}} = M_v \times L_v \tag{6}$$

where the mass loss due to vaporization can be expressed as:

$$M_v = m\sqrt{\frac{2\pi k_b T_s}{m}} \times P_{\text{amb}} \times \exp\left(\frac{\Delta H_v}{k_b T_v}\left(1 - \frac{T_v}{T_s}\right)\right) \tag{7}$$

2.1.3 Volumetric Heat Source

As outlined in the preceding sections, the thermal model adopted in this study neglected certain physical mechanisms, including melt pool convection and the interaction of laser energy with the powder bed, such as multiple internal reflections, which are likely to influence the evolution of melt pool morphology during L-PBF. To address this, a volumetric heat source was scaled using the experimentally observed melt pool depth. In the L-PBF process, the melt pool depth varies with changes in material properties and machine parameters. According to the literature, a normalized energy input-based analytical function can be constructed to obtain a scaling function for the experimentally measured melt pool depth [41–45]. This scaling function is formulated to include phenomenological factors such as laser intensity, laser absorption coefficient, laser interaction time, thermal diffusivity, specific heat, and melting temperature. Consequently, this volumetric heat formulation enables a reasonable approximation of the changes in melting mode and thermal profiles that occur with varying machine parameters and material properties. The following formulation describes the volumetric heat source [46]:

$$q''' = \frac{g\alpha P}{\pi r_b^2}\exp\left(-\frac{gr^2}{r_b^2}\right) f(z); \quad f(z) = \exp\left(-\frac{(z - Z_0)^2}{H^2}\right) \tag{8}$$

In the above formulation, the term H corresponds to the melt pool depth, which is scaled using the following normalized energy input-based analytical equation [41, 44]:

$$H = r_b \times A \times \left[\left(\frac{\alpha P}{\pi r_b^2}\right) \times \left(\frac{\tau}{\sqrt{\alpha_{th}\tau}}\right) \times \left(\frac{1}{\rho C_p T_s}\right)\right]^n, \quad \text{where } \tau = \frac{r_b}{V} \tag{9}$$

The parameters A and n are material fitting constants, which can be obtained by fitting the above equation with experimentally obtained melt pool depth values. Thus, the above set of equations completes the conduction-based heat transfer formulation of the L-PBF process. In this study, SS316L material system was considered. Note that α is the laser absorption coefficient. In the current framework, at any given point below the melting temperature, α has been assigned a value pertaining to powder bed absorption. In case the temperature exceeds the melting temperature, α has been assigned the value of the molten metal absorption coefficient. The values for powder bed and molten metal absorption coefficients were obtained from the literature for the material system SS316L [43]. The machine parameters and the values of the thermophysical properties used to evaluate Eqs. (1)–(9) are listed in Tables 2 and 3, respectively. Additionally, Eq.9 was fitted using melt pool depth data for the SS316L material obtained from in-house experiments. The fitted dataset is plotted in Figure 1 for reference, and the fitting constants are provided in Table 3 [39, 46–51].

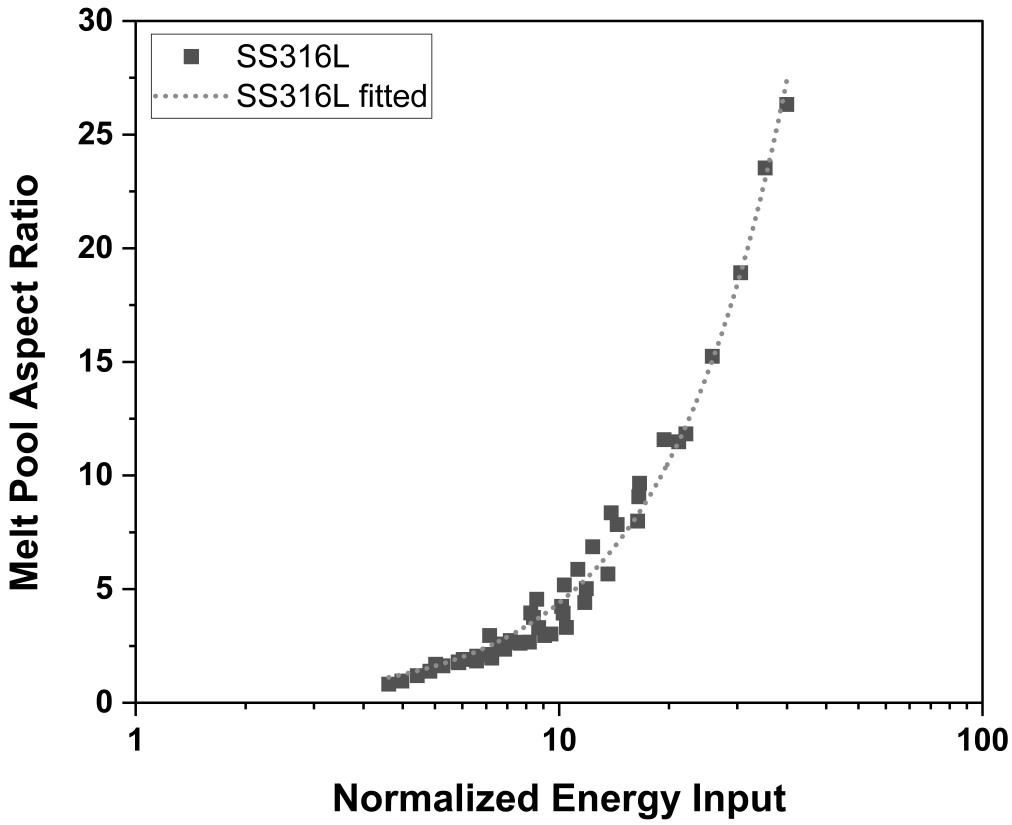


Fig. 1: Melt pool aspect ratio (H/r_b) as function of normalized energy input $\left(\alpha P \pi r_b^2 \times \sqrt{\frac{\tau_{\alpha th}}{\tau}} \times \frac{1}{\rho C_p T_s}\right)$ for SS316L.

The developed numerical framework was implemented within the commercial FEM software COMSOL Multiphysics®. To resolve the heating of the laser beam, an adaptive meshing strategy with quadrilateral mapped elements was employed. The minimum mesh size, determined through convergence analysis, ranged from 2 to 15 μm depending on the given process parameter set. The computations were performed on an Intel® Xeon® Gold 6252 CPU (2.10 GHz, 190 GB RAM) processor. Figure 2 presents the transverse cross-sections of numerically simulated melt pool geometries alongside the experimental results for all four material systems. The melt pool dimensions obtained from the numerical model, using the aforementioned analytical functions, are in strong agreement with the experimental data. Furthermore, the melt pool aspect ratio (depth-to-half-width ratio) predicted by the developed numerical model shows good correlation with the experimentally measured values (Figure 3). Within the current framework, the choice of experimental validation using the melt pool aspect ratio was based on the distinct melting modes observed in laser powder bed fusion. As reported in the literature, three melting modes exist during laser powder bed interaction: conduction, transition, and keyhole modes [33]. These melting modes are contingent on process parameters and dictate the coupling between the laser beam and the molten pool, which significantly influences the melt pool geometry and the evolved temperature within the molten zone.

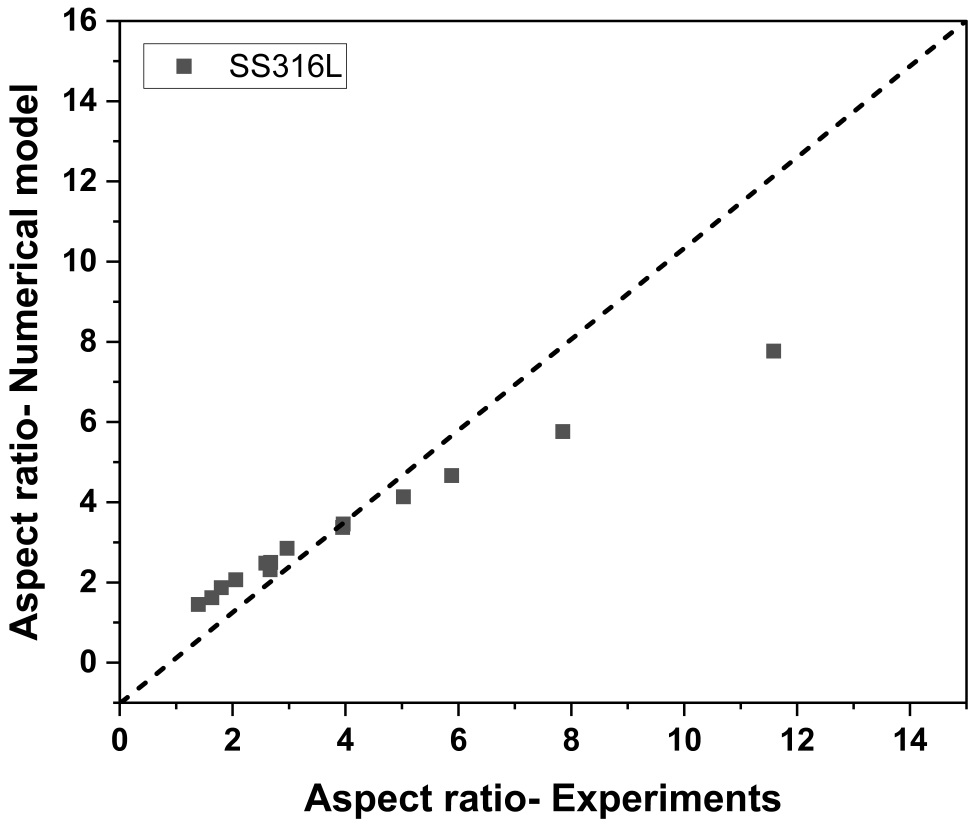


Fig. 2: Comparison of numerically simulated melt pool geometries with experimental results for SS316L.

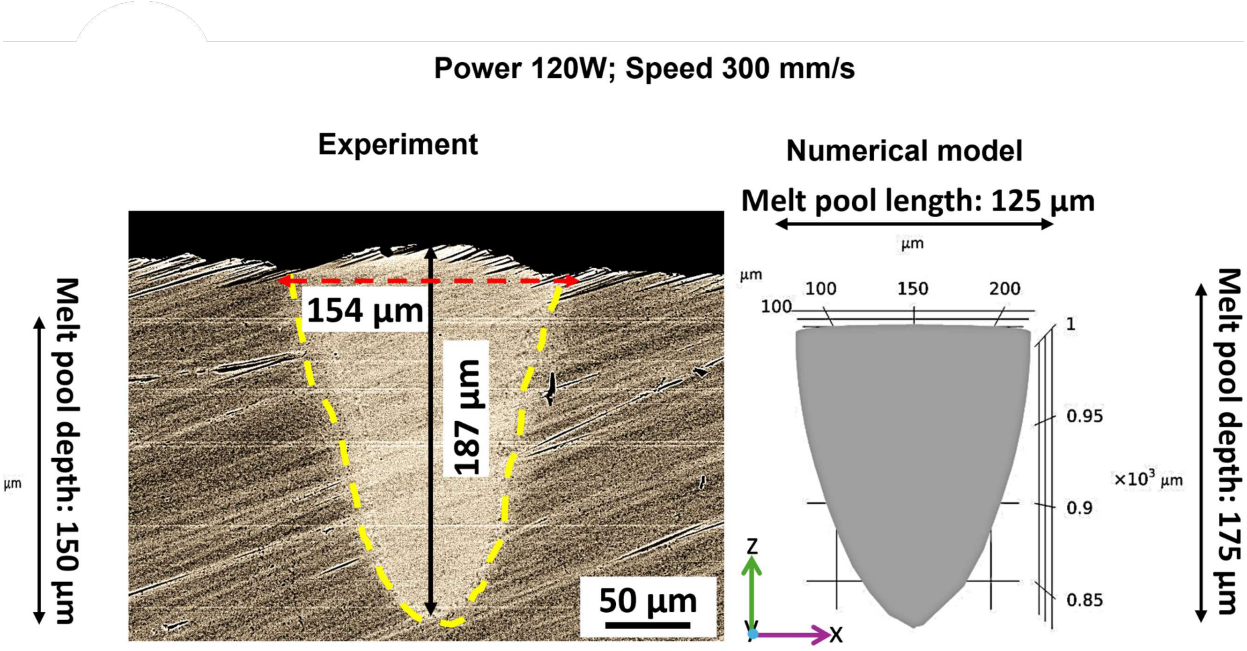


Fig. 3: Comparison of experimentally observed and numerical model based prediction of melt pool aspect ratios (H/r_b).

Given that the present framework considers the laser-matter interaction as a pure conduction problem with appropriate vaporization heat source and sink terms, an accurate estimation of the molten volume is essential to establish a reasonable representation of thermal evolution. Moreover, as suggested in the literature, the small diameter of the laser beam and the low laser interaction time (≤ 1 ms) pose challenges for experimental measurements of thermal evolution within the laser-matter interaction zone in L-PBF [33, 34].

In this context, the present framework, within its current limitations, provides reasonable validation in terms of the melt pool aspect ratio, effectively reflecting the prevailing melting mode, and the corresponding thermal evolution.

2.1.4 Experimental Method

In the present framework, the melt pool aspect ratio for the material system SS316L was evaluated through in-house experiments. For SS316L, single-track L-PBF experiments were conducted using a Trumpf TruPrint 1000 machine with a laser beam diameter of 55 μm. The SS316L powders, procured from ThermoFisher®, had a D_{50} particle size of 35 μm. The process parameters for SS316L material system is listed in Table 2.

Post-processing, the single-track specimens were cross-sectioned, polished, and subjected to metallographic analysis to determine the melt pool morphology (for aspect ratio calculation) using a Keyence VKS laser profilometer.

Table 2: Process parameters employed for SS316L dataset generation.

Parameter	**SS316L**
Laser Power (W)	100–250
Scanning Speed (m/s)	0.3–1.5
Hatch Spacing (mm)	0.05
Beam Radius (mm)	0.0275
Layer Thickness (mm)	0.05
Beam Adjustment Factor (g)	2.0
Time Step (s)	1×10^{-4}

Table 3: Thermophysical properties employed in the SS316L 3D heat transfer model.

Thermophysical Property	**SS316L** [47, 48]
Density, Solid (kg/m^3)	7950
Density, Liquid (kg/m^3)	$8200 - 0.77T$
Conductivity, Solid (W/(m·K))	$9.23 + 0.0139T$
Conductivity, Liquid (W/(m·K))	$5.5 + 0.0133T$
Specific Heat, Solid (J/(kg·K))	$415 + 0.01838T$
Specific Heat, Liquid (J/(kg·K))	830
Heat of Melting (kJ/mol)	15.5
Heat of Vaporization (kJ/mol)	380
Liquidus Temperature (K)	1723
Solidus Temperature (K)	1658
Vaporization Temperature (K)	3090
Boltzmann Constant (J/K)	1.328×10^{-23}
Convective Heat Transfer Coefficient (W/(m^2·K))	15
A, n	0.14, 1.47

2.2 Data Pre-processing

Training a neural network for LPBF involves massive differences in scale. The melt pool is extremely small and highly localized, but it contains steep and highly localized temperature gradients. Meanwhile, the surrounding solid metal stretches out much further and exhibits very slow, simple cooling behavior. Because of this massive difference in volume, the simulation dataset is highly imbalanced. To ensure the neural network successfully learns both the temperature behaviors, two critical preprocessing steps were applied: (a) global dataset normalization and (b) stratified sampling.

First, standardizing data on a per-simulation basis is ineffective for parametric models because changing the laser power P physically changes the overall temperature baseline. If normalized for each process parameter combination individually, the network would fail to learn how sensitive the temperature is to changes in power. Instead, we calculated global statistics ($\mu_{\text{global}}, \sigma_{\text{global}}$) across the entire combined dataset:

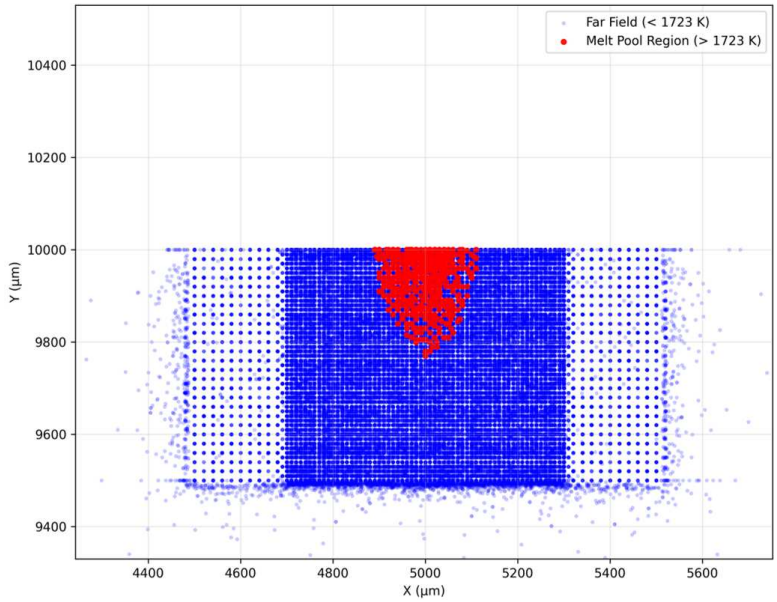


Fig. 4: Spatial visualization of the different thermal regions in the LPBF simulation. High-temperature points ($T > 1723\,K$) are confined to a microscopic melt pool core, while the vast majority of the simulation volume consists of slower diffusion and far-field cooling. This structural imbalance requires controlled training batches.

$$\hat{T} = \frac{T - \mu_{\text{global}}}{\sigma_{\text{global}}}, \qquad \hat{x}_i = 2 \cdot \frac{x_i - \min(x_i)}{\max(x_i) - \min(x_i)} - 1, \tag{10}$$

This ensures the neural network learns a consistent scale across the continuous parameter ranges of $P \in [100\,\text{W}, 250\,\text{W}]$ and $V \in [0.3\,\text{m/s}, 1.5\,\text{m/s}]$ for SS316L. These exact same scaling constants were locked in and used later for all predictions to maintain physical accuracy.

The second major challenge is the physical dominance of the far-field region. In the FEM data, more than 99% of the simulation volume is just solid metal slowly conducting background heat. The physically critical melt pool occupies only a tiny fraction of the space. Figure 4 highlights exactly where these different thermal regions are physically located underneath the laser.

If the neural network selects training points completely at random (uniform sampling), vast majority of its training time would be wasted looking at simple background conduction, causing it to fail inside the melt pool.

To fix this, a stratified sampling strategy was implemented. The dataset was categorized into three thermal zones: the Melt Pool, the Diffusion region, and the Far-Field. During training, the sampling algorithm was forced to construct custom mini-batches consisting of exactly 50% randomly drawn points, and 50% points pulled strictly from the high-temperature melt pool.

Figure 5 proves the mathematical impact of this approach. While a blind uniform pull practically ignores the melt pool (capturing it only 0.5% of the time), the stratified approach mathematically forces the training batches to dedicate half of their capacity to the melt pool laser physics, while preserving just enough background points to stabilize the surrounding boundaries.

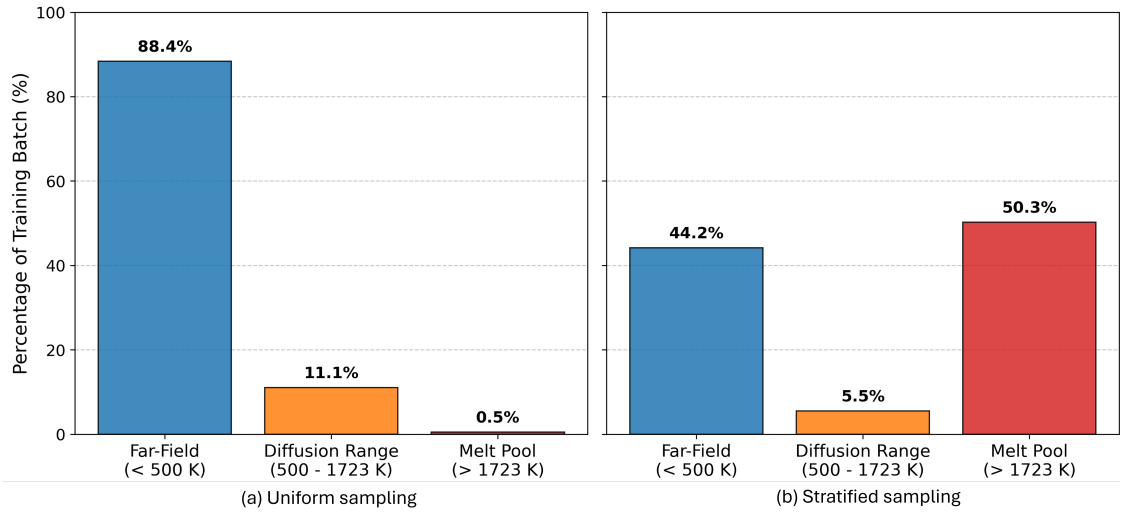


Fig. 5: Quantitative comparison of data batching strategies. (a) A standard uniform random pull overwhelmingly favors far-field data points and practically ignores extreme gradients. (b) The implemented stratified adaptive sampling algorithm guarantees that over 50% of every training batch is strictly dedicated to resolving the complex physics of the melt pool.

The dataset consisted of nine simulation cases spanning different combinations of laser power and scan speed. Six parameter combinations were used for model training and internally partitioned into training (95%) and validation (5%) subsets. The remaining three parameter combinations were completely excluded during training and reserved exclusively for evaluation.

These held-out cases were selected to represent distinct regions of the parameter space, including intermediate, boundary, and high energy-density operating regimes. Although the number of parameter combinations is limited, each simulation contains dense spatiotemporal thermal information across the full 3D domain. These data characteristics provide the foundation for learning continuous thermal behavior across unseen process conditions.

3 Methodology

3.1 Network Architecture

The proposed framework is designed as a parameterized data-driven neural network with physics-based regularization for predicting transient thermal fields in Laser Powder Bed Fusion (LPBF) across varying process conditions. Unlike conventional PINN formulations that solve the thermal field for a fixed set of process parameters, the proposed model directly incorporates process variables into the network input space, enabling continuous parametric learning across multiple operating conditions. Specifically, the network learns the mapping:

$$T_{pred} = f(x, y, z, t, P, V) \tag{11}$$

where (x, y, z, t) represent the spatiotemporal coordinates and (P, V) denote the laser power and scan speed, respectively. By embedding process parameters directly into the neural representation, the framework learns continuous thermal relationships across the bounded process space rather than memorizing individual simulation cases.

The parametric surrogate is explicitly designed as a hybrid data-driven model with physics-based regularization, rather than a classical rigid PINN. Because the 6D parameter space (x, y, z, t, P, V) contains dense supervision data but highly localized critical regions surrounding the melt pool, supervised learning provides the primary optimization signal, while the physics-based residual term acts as a thermodynamic regularizer. This hybrid formulation promotes physical consistency while ensuring stable convergence across the large computational domain. Such a design is particularly well-suited for LPBF thermal fields, where extreme thermal gradients are confined to a small fraction of the domain while the majority of the spatial region remains diffusion dominated.

The overall workflow of the proposed parameterized data-driven framework is illustrated in Fig. 6. The network receives the spatiotemporal coordinates and process parameters as inputs and predicts the corresponding temperature field. Automatic Differentiation (AD) is then utilized to compute the required derivatives of the predicted temperature field, which are subsequently incorporated into the governing heat conduction residual during training.

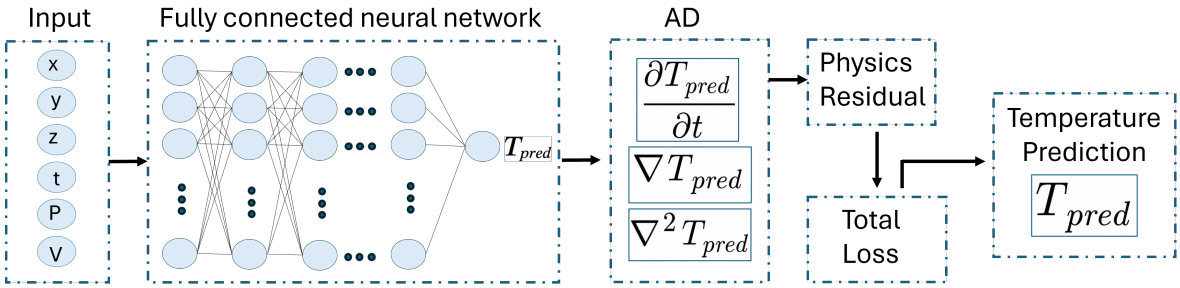


Fig. 6: Schematic overview of the proposed framework for transient thermal field prediction in LPBF. The framework integrates supervised thermal regression with physics-based residual regularization through automatic differentiation.

The architecture consists of a fully connected Multi-Layer Perceptron (MLP) with 6 input neurons corresponding to the spatiotemporal coordinates and process parameters. To ensure mathematical stability, all inputs and outputs were globally standardized as detailed in the Data Pre-Processing section, preserving continuous cross-parameter sensitivities. Output predictions are rescaled back to dimensional Kelvin (K) prior to evaluating the PDE residual, ensuring that the governing equations remain strictly dimensional. This separation avoids numerical stiffness in the PDE residual while maintaining stable gradient propagation in the supervised loss.

The network comprises 8 densely connected hidden layers, each containing 256 neurons, yielding approximately 460,000 trainable parameters. Rectified Linear Unit (ReLU) activations were utilized. While ReLU activations are known to limit strictly continuous second-order derivatives, they were empirically selected due to their ability to prevent vanishing gradients and provide faster, more robust convergence when resolving highly localized thermal gradients near melt pool boundaries. In the present formulation, the PDE residual primarily benefits from first-order temporal gradients and localized spatial transitions, for which ReLU provides sufficient representational capacity while maintaining stable optimization behavior.

The training objective includes terms corresponding to both supervised data fidelity and physics-based consistency:

$$\mathcal{L} * total = \mathcal{L} * data + \lambda_{PDE} \cdot \mathcal{L}_{PDE} \tag{12}$$

The data fidelity term ($\mathcal{L} * data$) enforces regression to the finite element simulation data using Mean Squared Error (MSE):

$$\mathcal{L} * data = \frac{1}{N_{data}} \sum_{i=1}^{N_{data}} |T_{pred}(\mathbf{x} * i) - T * true(\mathbf{x} * i)|^2 \tag{13}$$

where $T*true$ represents the normalized ground truth temperature. The supervised dataset N_{data} is sampled directly from the high-fidelity FEM thermal simulations, which inherently contain the boundary condition (BC) and initial condition (IC) information. As a result, BCs and ICs are implicitly enforced through the supervised regression process, eliminating the need for additional explicit penalty terms.

The physics loss ($\mathcal{L}_{PDE}$) measures the residual of the transient heat conduction equation, defined using dimensional quantities:

$$\mathcal{R} = \rho C_p \frac{\partial T}{\partial t} - \nabla \cdot (k \nabla T) - Q(x, y, z, t) \tag{14}$$

where ρ, C_p, and k denote the material density, specific heat, and thermal conductivity, respectively.

Automatic Differentiation (AD) is employed to compute the derivatives of the predicted temperature field directly from the neural network output:

$$\frac{\partial T_{pred}}{\partial t}, \qquad \nabla T_{pred}, \qquad \nabla^2 T_{pred} \tag{15}$$

These derivatives are subsequently substituted into the governing PDE residual, enabling fully differentiable physics-based regularization during network optimization.

To accurately capture the moving heat source without temporal interpolation artifacts, the residual is evaluated in a local coordinate frame attached to the laser center $(X_c(t), Y_0, Z_0)$:

$$X_c(t) = X_0 + V \cdot t \tag{16}$$

The volumetric heat source Q is modeled as a 3D Gaussian distribution:

$$Q = \frac{g\alpha P}{\pi H r_b^2} \exp\left(-g\frac{(x - X_c(t))^2 + (y - Y_0)^2}{r_b^2}\right) \exp\left(-\frac{(z - Z_0)^2}{H^2}\right) \tag{17}$$

Note that the above equation is an expanded form of $Eq.8$, where the melt pool depth, H for each of the concerned process parameters were calculated based on $Eq.9$ The PDE loss is computed as the mean squared residual evaluated over the input points sampled:

$$\mathcal{L} * PDE = \frac{1}{N * PDE} \sum_{j=1}^{N_{PDE}} \left|\mathcal{R}(\mathbf{x}_j)\right|^2 \tag{18}$$

The PDE evaluation points are sampled using the same stratified importance sampling distribution as the supervised dataset, with a 1:1 ratio between N_{data} and N_{PDE}. Unlike uniform random sampling, which disproportionately favors the diffusion-dominated far-field region, the implemented stratified sampling strategy intentionally increases representation near the melt pool where thermal gradients and PDE curvature are most significant. This improves sensitivity to localized thermodynamic inconsistencies while maintaining sufficient coverage across the global domain.

The regularization weight λ_{PDE} was set to 1×10^{-4} during physics-regularized training. Since the supervised FEM dataset densely resolves the thermal field, the data loss serves as the primary optimization objective, while the PDE residual acts as a secondary physics-based regularizer. The weighting parameter λ_{PDE} controls the influence of the PDE residual relative to the supervised loss. Preliminary experiments showed that significantly larger values destabilized optimization due to imbalance between the derivative-based residual terms and the supervised gradients, while smaller values reduced the influence of the physics constraint.

3.2 Model Training Strategy

Training a single network to simultaneously resolve both the highly localized melt pool region and the low-gradient diffusion tail across a continuous parameter space presents significant optimization challenges due to the inherently multi-scale nature of LPBF thermal fields. To improve training stability, a two-phase curriculum learning strategy is adopted, separating data-driven learning from subsequent physics-regularized fine-tuning.

The first phase establishes a robust approximation of the thermal field solely from the high-fidelity FEM data. During this stage, the PDE regularization term is effectively disabled by setting $\lambda_{PDE} \approx 0$, allowing the network to minimize only the supervised regression loss $\mathcal{L}_{data}$. This phase enables the network to learn the dominant thermal structure and parameter-dependent relationships directly from data without the additional computational complexity associated with derivative-based residual evaluation. Furthermore, it provides a well-conditioned initialization for the subsequent physics-regularized optimization stage.

Phase I is trained for 100 epochs using the Adam optimizer with a learning rate of 1×10^{-4} and a batch size of 8,192 per GPU.

In the second phase, the PDE residual term is activated to refine the learned thermal manifold and improve thermodynamic consistency. The trained weights from Phase I are used as initialization, and the regularization parameter λ_{PDE} is introduced and set to 1×10^{-4}. Rather than acting as the dominant optimization objective, the PDE residual functions as a physics-guided correction mechanism that encourages consistency with the local energy balance equation in regions between sampled data points. This additional regularization improves interpolation behavior and strengthens generalization across unseen parameter combinations within the bounded process space.

Phase II continues for an additional 100 epochs using the same optimizer configuration to maintain stable convergence behavior. Due to the density of the FEM supervision dataset, the supervised loss remains the dominant training signal throughout optimization, while the PDE residual provides a secondary physics-based constraint. This staged optimization strategy improves overall training stability by preventing early imbalance between the supervised and derivative-based physics loss terms.

4 Experimental Results

The predictive performance of the proposed framework was evaluated using three process-parameter combinations that were completely excluded during training. These held-out cases represent distinct thermophysical regimes within the bounded process space, including intermediate, boundary, and high energy-density operating conditions. It should be noted that the proposed framework is intended to learn

continuous interpolation across unseen combinations of laser power and scan speed within the trained thermophysical domain, rather than unrestricted extrapolation to arbitrary process conditions, geometries, or materials.

Across these unseen parameter combinations, the model achieved a global Root Mean Squared Error (RMSE) of $9.01, \mathrm{K}$ and Mean Absolute Error (MAE) of $3.01, \mathrm{K}$ (Table 4), indicating strong agreement with the FEM-computed thermal histories across both localized melt pool regions and diffusion-dominated far-field regions.

Beyond mean-error statistics, the absolute error distribution remains strongly concentrated, with a 95^{th} percentile absolute error of $8.98, \mathrm{K}$. Larger absolute deviations remain primarily localized near the moving laser source, where thermal curvature and temperature gradients are highest. This behavior is consistent with the underlying thermal physics of LPBF, where sharp localized gradients are confined near the melt pool core rather than distributed uniformly across the computational domain.

4.1 3D Melt Pool Morphology

To evaluate generalization across unseen process conditions, predicted 3D melt pool morphologies were directly compared against FEM solutions for three parameter combinations excluded during training. Figure 7 presents visual comparisons across three representative regimes: a low-power configuration $(175, \mathrm{W}, 0.3, \mathrm{m/s})$, a high energy-density configuration $(250, \mathrm{W}, 0.3, \mathrm{m/s})$, and a high-speed configuration $(250, \mathrm{W}, 0.9, \mathrm{m/s})$.

The 3D isosurfaces were extracted at the liquidus temperature threshold ($T = 1723, \mathrm{K}$), corresponding to the physical melt pool boundary. Across all three regimes, the model accurately reconstructs the elongated melt pool morphology observed in the FEM results. The relative error maps indicate that deviations remain primarily localized within the high-temperature interior region of the melt pool, where thermal gradients are steepest. Importantly, the liquidus boundary itself, which governs the effective melt pool geometry, is recovered with minimal deviation across all held-out parameter combinations.

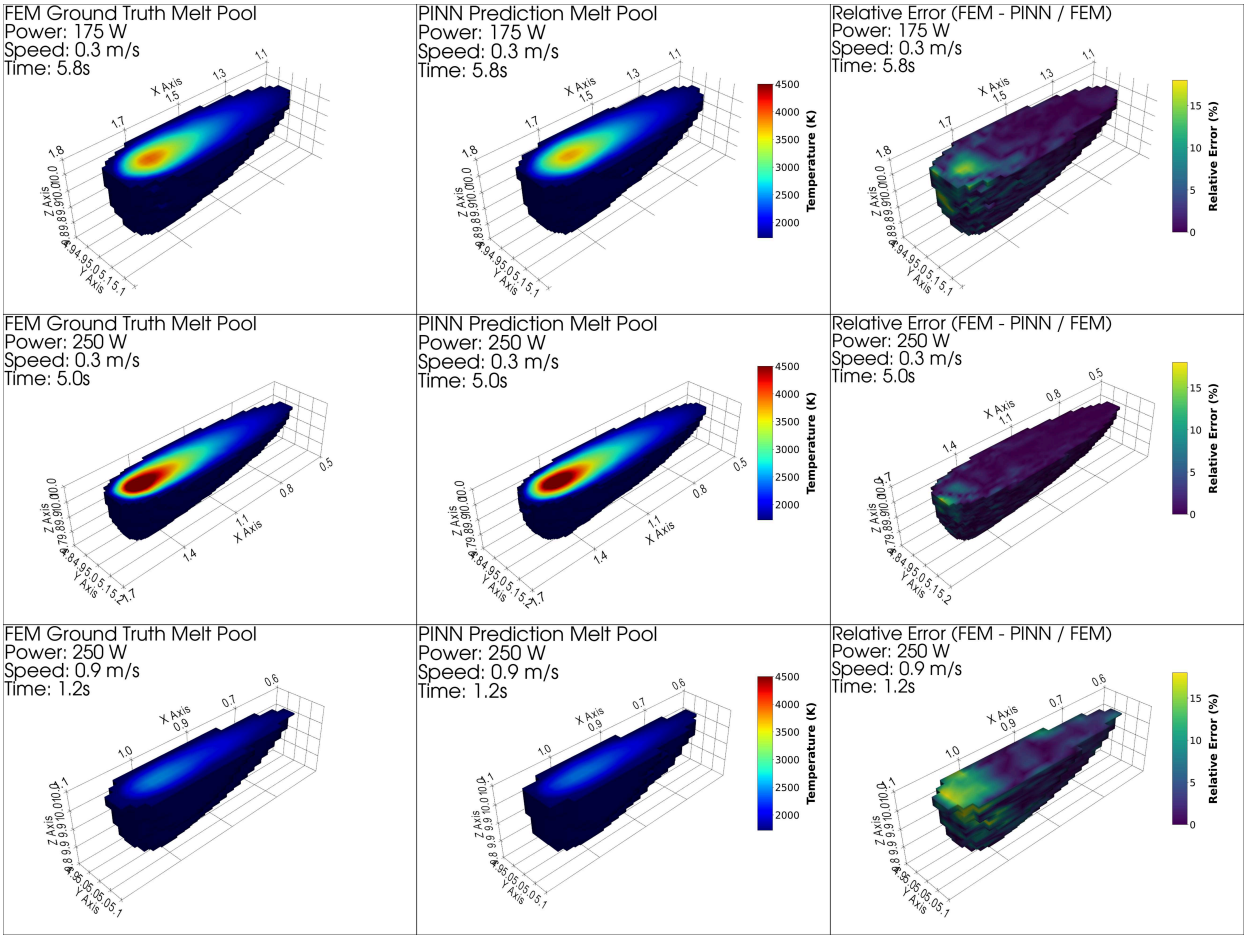


Fig. 7: Three-dimensional melt-pool visualization across varying power and speed regimes. FEM ground truth (left column), Model predictions (center column), and internal relative error (right column). The melt pool boundary is extracted using a liquidus temperature threshold of $T = 1723, \mathrm{K}$, demonstrating preservation of the metallurgically relevant melt-pool geometry across unseen process conditions.

4.2 Quantitative Validation of Melt Pool Dimensions

To quantify geometric fidelity beyond scalar temperature metrics, the physical melt pool dimensions (Length, Width, and Depth) were extracted for the three held-out process configurations.

As illustrated in Figure 8, the predicted melt pool dimensions remain in close agreement with the FEM reference solutions across all evaluated operating conditions. The framework captures physically consistent trends associated with changes in process parameters, including the reduction in melt pool length with increasing scan speed and the variation in penetration depth with laser power. These results indicate that localized smoothing near peak temperatures does not significantly affect the macroscopic geometric characteristics relevant to additive manufacturing process analysis.

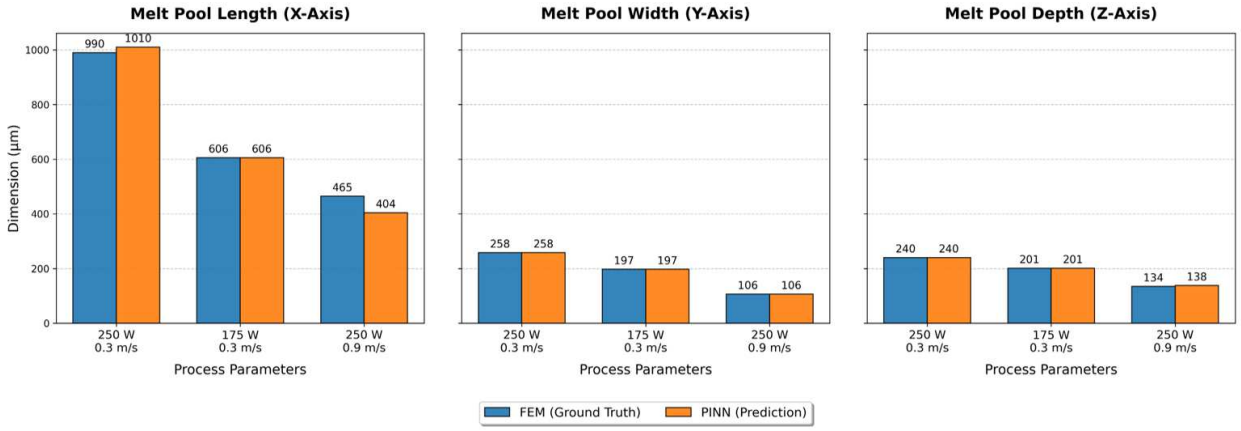


Fig. 8: Quantitative comparison of melt pool dimensions. The extracted geometric bounds of the $1723, \mathrm{K}$ isosurface demonstrate preservation of physically consistent melt-pool scaling behavior across varying process conditions.

4.3 Gradient Fidelity Along the Melt Pool Core

Because neural surrogates are known to exhibit spectral bias that can smooth highly localized gradients, fidelity was further evaluated using one-dimensional line profiles through the center of the melt pool. To assess generalization behavior under high-gradient thermal conditions, this validation was performed using the highest thermal intensity node identified within the unseen test dataset $(250, \mathrm{W}, 0.3, \mathrm{m/s}, t = 1.03, \mathrm{s})$.

Figure 9 illustrates continuous 1D line profiles extracted along both the longitudinal (scan) axis and the depth (penetration) axis. The model captures the gradient structure with strong agreement in both peak location and thermal decay along the scan direction. In the depth direction, slight smoothing near the peak temperature is observed, reflecting the increased difficulty associated with approximating highly localized thermal variations within the melt pool core. This behavior is consistent with known neural network spectral bias, where sharp high-gradient regions may exhibit moderate smoothing near localized extrema. Nevertheless, both profiles demonstrate that the model preserves the dominant anisotropic characteristics of the thermal field without exhibiting significant large-scale smoothing artifacts.

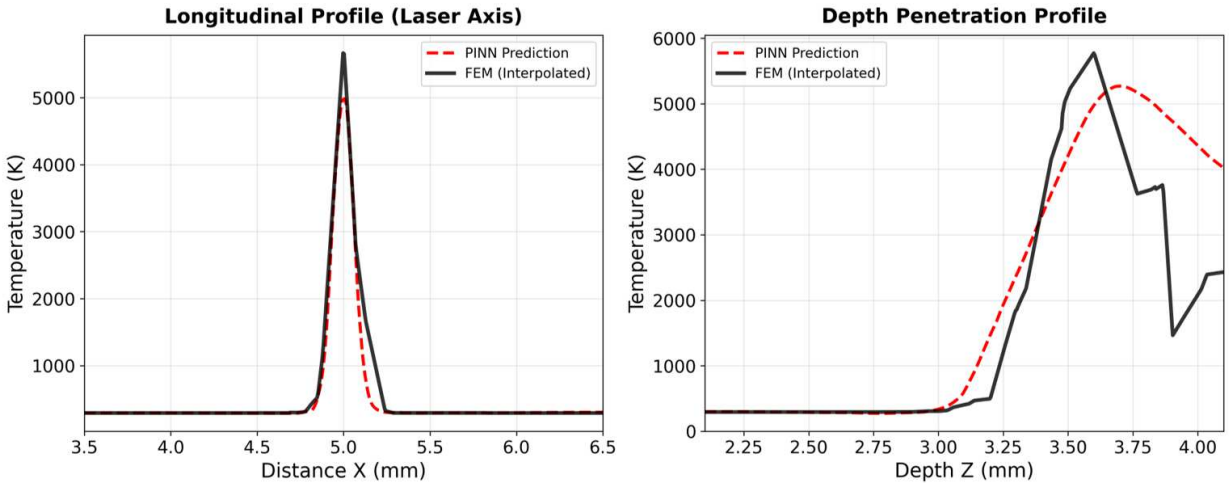


Fig. 9: Anisotropic thermal cross-sections through the melt pool core. (Left) Longitudinal profile along the laser scanning axis. (Right) Depth penetration profile extending into the substrate. The dashed red line represents the model prediction compared against interpolated FEM samples (black), demonstrating preservation of the dominant thermal gradient structure.

To further evaluate performance across varying thermal regimes, the prediction error was analyzed as a function of FEM temperature rather than spatial position alone. Table 4 summarizes this temperature-conditioned accuracy.

The far-field region ($T \leq 1723, \mathrm{K}$), governed primarily by diffusion-dominated conduction, is predicted with an RMSE of $5.99, \mathrm{K}$. In contrast, the melt-pool region ($T > 1723, \mathrm{K}$) exhibits a higher absolute RMSE of $93.91, \mathrm{K}$. However, when normalized relative to the peak process temperatures (approaching $5700, \mathrm{K}$), this corresponds to a relative error of only 1.64%. This indicates that although absolute deviations naturally increase near regions with steep thermal gradients and large temperature magnitudes, the relative predictive fidelity remains strong within the melt pool regime.

Table 4: Quantitative performance metrics evaluated on the held-out test set. The 95^{th} percentile error indicates that most predictions remain within single-digit Kelvin deviation, while larger absolute errors remain localized near the high-gradient melt-pool region.

Metric	**Value**
Global RMSE	9.01 K
Mean Absolute Error (MAE)	3.01 K
95th Percentile Absolute Error	**8.98 K**
Melt-Pool RMSE ($T > 1723$ K)	93.91 K
Melt-Pool Relative Error	**1.64%**
Far-Field RMSE ($T \leq 1723$ K)	5.99 K

The temperature-conditioned error trend is shown in Figure 10, where RMSE is mapped across ascending FEM temperature bins. The vertical dashed marker at $1723, \mathrm{K}$ denotes the liquidus threshold utilized during stratified sampling, separating the diffusion-dominated solid region from the melt-pool regime.

A gradual increase in absolute RMSE is observed at elevated temperatures beyond this threshold. This trend reflects the progressively sharper spatial curvature of the thermal field near the moving heat source. Because the melt pool occupies a highly localized spatial region with steep temperature gradients, relatively small positional deviations in the predicted thermal field can produce larger absolute temperature differences. Importantly, this increase in absolute RMSE does not indicate global instability or failure of the thermal prediction framework. As reflected by the 1.64% relative error within the melt-pool regime, the model continues to preserve the dominant thermal energy distribution with strong consistency.

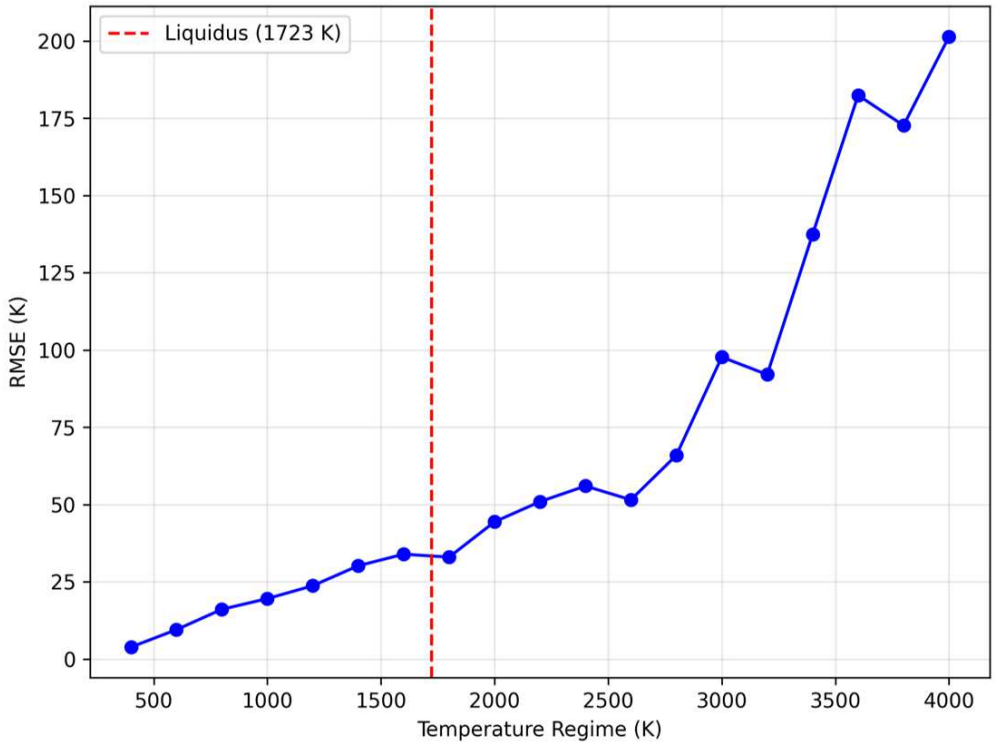


Fig. 10: RMSE conditioned on FEM temperature bins. The vertical line marks the liquidus-temperature transition separating far-field diffusion behavior from the melt-pool regime. The increase in absolute RMSE at elevated temperatures primarily reflects increasing thermal curvature near the moving laser source.

Figure 11 presents the evolution of the training and validation losses throughout optimization. Both metrics decrease smoothly and remain closely aligned throughout training, indicating stable optimization behavior despite the multi-scale nature of the thermal field.

The absence of significant divergence or oscillatory behavior in the loss curves suggests that the combination of global normalization, stratified sampling, and staged physics-based regularization contributed to a well-conditioned optimization process across the sampled 6D parameter space.

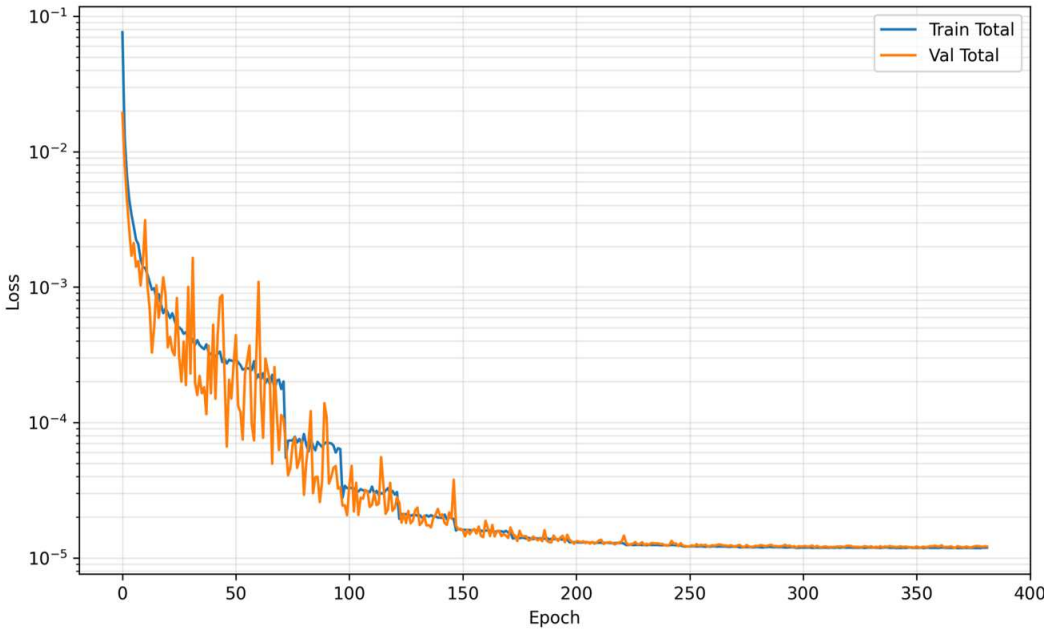


Fig. 11: Training convergence history (log scale). Closely aligned training and validation losses indicate stable optimization behavior throughout the training process.

5 Conclusion

This study presents a parameterized data-driven neural network framework with physics-based regularization for predicting transient thermal fields in Laser Powder Bed Fusion for SS316L across continuous process parameters. By incorporating process variables directly into the input space, the framework learns a continuous parametric relationship between process conditions and thermal response, addressing the limitations of conventional PINN formulations that are typically restricted to fixed operating conditions.

The proposed hybrid formulation combines dense data-driven supervision with physics-based regularization, enabling stable learning across a highly imbalanced and multi-scale thermal domain. Key design strategies, including stratified sampling and global normalization, improve representation of both the localized melt pool region and the diffusion-dominated far field while preserving physically meaningful scaling relationships across varying process conditions.

Extensive validation demonstrates that the framework maintains strong predictive agreement across parameter combinations excluded during training, accurately reconstructing temperature distributions, melt pool geometry, and dominant thermal gradients. While larger absolute deviations are observed near the melt pool core, this behavior is associated with the sharply localized thermal curvature near the moving laser source rather than a loss of overall predictive consistency.

The results further indicate that the framework learns continuous relationships between process parameters and thermal response within the bounded training domain, rather than memorizing individual simulation cases. Combined with dense spatiotemporal supervision and physics-based regularization, the proposed framework provides a scalable and physically consistent surrogate model suitable for rapid process exploration and digital twin applications in additive manufacturing.

Future work will focus on improving resolution within highly localized thermal regions through adaptive sampling strategies and exploring alternative neural architectures capable of better resolving steep thermal gradients while maintaining computational scalability. Extensions to broader process windows, larger parameter spaces, and additional multiphysics effects may further improve the applicability of the framework for additive manufacturing digital twin development.

Author statement. The corresponding author (Narendra B Dahotre), on behalf of all the authors of this submission, declare that there are no financial and personal relationships with other people or organizations that could inappropriately influence this work.

CRediT authorship contribution statement. **Aishwarya Manjunath**: Writing – original draft, Methodology, Data processing, ML modeling, Conceptualization. **Hang Tran**: Writing – review & editing **Selvamurugan Palaniappan**: Writing – review & editing, FEM modeling. **Shashank Sharma**: Writing – review & editing, Methodology, Validation, Formal analysis, FEM modeling, Conceptualization. **Song Fu**: Writing – review & editing, Supervision. **Narendra B Dahotre**: Writing – review & editing, Validation, Supervision, Project administration, Investigation, Formal analysis.

Declaration of Competing Interest. The authors declare that they have no known competing financial interests or personal relationships that could have appeared to influence the work reported in this paper.

- **Funding**: Narendra B. Dahotre reports financial support was provided by State of Texas Appropriations: 190405-105-805008-220.
- **Conflict of interest/Competing interests**: The authors declare that they have no known competing financial interests or personal relationships that could have appeared to influence the work reported in this paper.
- **Ethics approval and consent to participate**: Not applicable.
- **Consent for publication**: Yes.
- **Data availability**: Data will be made available on request.
- **Materials availability**: Not applicable.
- **Code availability**: Code will be made available on request.

Acknowledgments. Authors acknowledge the Center for Agile and Adaptive Additive Manufacturing (CAAAM) funded through State of Texas Appropriation: 190405-105-805008-220 for the infrastructure support, and Materials Research Facility (MRF) at the University of North Texas for the microscopy work.

Data Availability. Data will be made available on request.

References

[1] DebRoy, T., Wei, H.L., Zuback, J.S., Mukherjee, T., Elmer, J.W., Milewski, J.O., Beese, A.M., Wilson-Heid, A.d., De, A., Zhang, W.: Additive manufacturing of metallic components–process, structure and

properties. Progress in Materials Science **92**, 112–224 (2018) https://doi.org/10.1016/j.pmatsci.2017.10.001

[2] Gordon, J.V., Narra, S.P., Cunningham, R.W., Liu, H., Chen, H., Suter, R.M., Beuth, J.L., Rollett, A.D.: Defect structure process maps for laser powder bed fusion additive manufacturing. Additive Manufacturing **36**, 101552 (2020) https://doi.org/10.1016/j.addma.2020.101552

[3] Ness, K.L., Paul, A., Sun, L., Zhang, Z.: Towards a generic physics-based machine learning model for geometry invariant thermal history prediction in additive manufacturing. Journal of Materials Processing Technology **302**, 117472 (2022) https://doi.org/10.1016/j.jmatprotec.2021.117472

[4] Patel, D., Sharma, R., Guo, Y.: Computational, data-driven, and physics-informed machine learning approaches for microstructure modeling in metal additive manufacturing. Annual Review of Heat Transfer **28** (2025)

[5] Jiang, F., Xia, M., Hu, Y.: Physics-informed machine learning for accurate prediction of temperature and melt pool dimension in metal additive manufacturing. 3D Printing and Additive Manufacturing **11**(4), 1679–1689 (2024)

[6] Ho, S., Zhang, W., Young, W., Buchholz, M., Al Jufout, S., Dajani, K., Bian, L., Mozumdar, M.: Dlam: Deep learning based real-time porosity prediction for additive manufacturing using thermal images of the melt pool. IEEE Access **9**, 115100–115114 (2021) https://doi.org/10.1109/ACCESS.2021.3105362

[7] Zhan, J., Li, Y., Guo, Z., Ma, R., Wang, S., Yang, X., Jarlöv, A., Cao, H., Lin, F., Xu, Y., Li, K., Zhang, Y.-W., Zhou, K.: A 4d-printed niti alloy with encoded microstructures evades the cooling capacity–energy efficiency trade-off in elastocaloric refrigeration. Materials Science and Engineering: R: Reports **169**, 101191 (2026) https://doi.org/10.1016/j.mser.2026.101191

[8] Zhan, J., Li, K., Ma, R., Zhu, L., Fang, J., Cao, H., Zhang, D.Z., Murr, L.E.: Achieving fine tailoring of elastocaloric properties of laser powder bed-fused niti alloy via laser beam manipulation. International Journal of Machine Tools and Manufacture **202**, 104210 (2024) https://doi.org/10.1016/j.ijmachtools.2024.104210

[9] Li, K., Fang, J., Zhan, J., Ma, R., Wang, S., Yang, X., Zhang, D.Z., Murr, L.E., Cao, H.: Elastocaloric effect of laser powder bed fused niti alloy with customizable hierarchical heterogeneous microstructure. Additive Manufacturing **97**, 104619 (2025)

[10] Xiong, Z., Li, H., Yang, H., Yang, Y., Liu, Y., Cui, L., Li, X., Masseling, L., Shen, L., Hao, S.: Micro laser powder bed fusion of niti alloys with superior mechanical property and shape recovery function. Additive Manufacturing **57**, 102960 (2022)

[11] Xie, J., Chai, Z., Xu, L., Ren, X., Liu, S., Chen, X.: 3d temperature field prediction in direct energy deposition of metals using physics informed neural network. The International Journal of Advanced Manufacturing Technology **119**(5), 3449–3468 (2022) https://doi.org/10.1007/s00170-021-08542-w

[12] Palaniappan, S., Krishna, K.M., Radhakrishnan, M., Sharma, S., Ramalingam, M.S., Banerjee, R., Dahotre, N.B.: Thermokinetics driven microstructure and phase evolution in laser-based additive manufacturing of ti-25wt.% nb and its performance in physiological solution. Materialia, 102190 (2024) https://doi.org/10.1016/j.mtla.2024.102190

[13] Zhou, Z., Shen, H., Liu, B., Du, W., Jin, J.: Thermal field prediction for welding paths in multi-layer gas metal arc welding-based additive manufacturing: A machine learning approach. Journal of Manufacturing Processes **64**, 960–971 (2021) https://doi.org/10.1016/j.jmapro.2021.02.033

[14] Sharma, R., Guo, Y.: Thermal-mechanical physics informed deep learning for fast prediction of thermal stress evolution in laser metal deposition. arXiv preprint arXiv:2412.18786 (2024)

[15] Hemmasian, A., Ogoke, F., Akbari, P., Malen, J., Beuth, J., Farimani, A.B.: Surrogate modeling of melt pool temperature field using deep learning. Additive Manufacturing Letters **5**, 100123 (2023) https://doi.org/10.1016/j.addlet.2023.100123

[16] Xu, S., Rai, R., Moore, R.D., Orlandi, G., Abdeljawad, F.: Mptp-net: melt pool temperature profile network for thermal field modeling in beam shaping of laser powder bed fusion. Journal of Intelligent

Manufacturing, 1–17 (2024) https://doi.org/10.1007/s10845-024-02449-5

[17] Anantatamukala, A., Krishna, K.M., Dahotre, N.B.: Generative adversarial networks assisted machine learning based automated quantification of grain size from scanning electron microscope back scatter images. Materials Characterization **206**, 113396 (2023) https://doi.org/10.1016/j.matchar.2023.113396

[18] S, K., Durgadevi, M.: Generative adversarial network (gan): a general review on different variants of gan and applications. In: 2021 6th International Conference on Communication and Electronics Systems (ICCES), pp. 1–8 (2021). https://doi.org/10.1109/ICCES51350.2021.9489160

[19] Cao, Z., Liu, Q., Liu, Q., Yu, X., Kruzic, J.J., Li, X.: A machine learning method to quantitatively predict alpha phase morphology in additively manufactured ti-6al-4v. npj Computational Materials **9**(1), 195 (2023) https://doi.org/10.1038/s41524-023-01152-y

[20] Hsu, T., Epting, W.K., Kim, H., Abernathy, H.W., Hackett, G.A., Rollett, A.D., Salvador, P.A., Holm, E.A.: Microstructure generation via generative adversarial network for heterogeneous, topologically complex 3d materials. Jom **73**, 90–102 (2021) https://doi.org/10.1007/s11837-020-04484-y

[21] Manjunath, A., Karri, V.M.K., Anantatamukala, A., Palaniappan, S., Sharma, S., Fu, S., Dahotre, N.B.: Machine learning-based prediction of thermal profiles during laser-based additive manufacturing. The International Journal of Advanced Manufacturing Technology **143**(5), 3159–3176 (2026) https://doi.org/10.1007/s00170-026-17732-3

[22] Guo, S., Agarwal, M., Cooper, C., Tian, Q., Gao, R.X., Grace, W.G., Guo, Y.: Machine learning for metal additive manufacturing: Towards a physics-informed data-driven paradigm. Journal of Manufacturing Systems **62**, 145–163 (2022) https://doi.org/10.1016/j.jmsy.2021.11.003

[23] Ren, K., Chew, Y., Zhang, Y., Fuh, J., Bi, G.: Thermal field prediction for laser scanning paths in laser aided additive manufacturing by physics-based machine learning. Computer Methods in Applied Mechanics and Engineering **362**, 112734 (2020) https://doi.org/10.1016/j.cma.2019.112734

[24] Hosseini, E., Scheel, P., Müller, O., Molinaro, R., Mishra, S.: Single-track thermal analysis of laser powder bed fusion process: Parametric solution through physics-informed neural networks. Computer Methods in Applied Mechanics and Engineering **410**, 116019 (2023) https://doi.org/10.1016/j.cma.2023.116019

[25] Gnanasambandam, R.: Physics-informed machine learning for digital twins of metal additive manufacturing. PhD thesis, Virginia Tech (2024). https://vtechworks.lib.vt.edu/items/4774481b-0c70-49a8-98ae-565ba97f1414

[26] Sharma, R., Guo, Y.: Physics-informed machine learning of thermal stress evolution in laser metal deposition. In: TMS Annual Meeting & Exhibition, pp. 550–559 (2025). Springer

[27] Sharma, R., Raissi, M., Guo, Y.: Physics-informed machine learning for smart additive manufacturing. Procedia CIRP **138**, 650–655 (2026)

[28] Depaoli, F., Felicioni, S., Ponzio, F., Aliberti, A., Macii, E., Bondioli, F., Padovano, E., Di Cataldo, S.: Physics-informed neural networks: a step towards data-driven optimization of additive manufacturing. In: 2024 IEEE 29th International Conference on Emerging Technologies and Factory Automation (ETFA), pp. 1–4 (2024). IEEE

[29] Zobeiry, N., Humfeld, K.D.: A physics-informed machine learning approach for solving heat transfer equation in advanced manufacturing and engineering applications. Engineering Applications of Artificial Intelligence **101**, 104232 (2021)

[30] Sajadi, P., Dehaghani, M.R., Tang, Y., Wang, G.G.: Two-dimensional temperature field prediction with in-situ data in metal additive manufacturing using physics-informed neural networks. Engineering Applications of Artificial Intelligence **150**, 110636 (2025)

[31] Chen, Z., Mu, H., He, F., Yuan, L., Zhu, H., Ma, N., Pan, Z.: A physics-informed machine learning approach for temperature field prediction in metallic additive manufacturing. Journal of Industrial Information Integration **47**, 100899 (2025)

[32] Faegh, M., Ghungrad, S., Haghighi, A.: A physics-informed neural network framework for decomposition and path planning in multi-laser additive manufacturing. Manufacturing Letters **44**, 1129–1138 (2025)

[33] Dahotre, N.B., Pantawane, M.V., Sharma, S. (eds.): Laser-based Additive Manufacturing: Modeling, Simulation, and Experiments. Wiley-VCH GmbH, Weinheim, Germany (2022). https://doi.org/10.1002/9783527828814

[34] Sharma, S., Joshi, S.S., Pantawane, M.V., Radhakrishnan, M., Mazumder, S., Dahotre, N.B.: Multiphysics multi-scale computational framework for linking process–structure–property relationships in metal additive manufacturing: A critical review. International Materials Reviews **68**(12), 943–1009 (2023) https://doi.org/10.1080/09506608.2023.2169501

[35] Patel, S., Vlasea, M.: Melting modes in laser powder bed fusion. Materialia **9**, 100591 (2020) https://doi.org/10.1016/j.mtla.2020.100591

[36] Parsazadeh, M., Sharma, S., Dahotre, N.: Towards the next generation of machine learning models in additive manufacturing: A review of process dependent material evolution. Progress in Materials Science (2023) https://doi.org/10.1016/j.pmatsci.2023.101102

[37] Moges, T., Ameta, G., Witherell, P.: A review of model inaccuracy and parameter uncertainty in laser powder bed fusion models and simulations. Journal of Manufacturing Science and Engineering, Transactions of the ASME **141** (2019) https://doi.org/10.1115/1.4042789/475003

[38] Ross, A.J., Bitharas, I., Perkins, K.G., Moore, A.J.: Volumetric heat source calibration for laser powder bed fusion. Additive Manufacturing **60**, 103267 (2022) https://doi.org/10.1016/j.addma.2022.103267

[39] Mukherjee, T., Wei, H.L., De, A., DebRoy, T.: Heat and fluid flow in additive manufacturing – part ii: Powder bed fusion of stainless steel, and titanium, nickel and aluminum base alloys. Computational Materials Science **150**, 369–380 (2018) https://doi.org/10.1016/j.commatsci.2018.04.027

[40] Pantawane, M.V., Sharma, S., Sharma, A., Dasari, S., Banerjee, S., Banerjee, R., Dahotre, N.B.: Coarsening of martensite with multiple generations of twins in laser additively manufactured ti6al4v. Acta Materialia **213** (2021) https://doi.org/10.1016/j.actamat.2021.116954

[41] Zagade, P., Gautham, B.P., De, A., DebRoy, T.: Analytical estimation of fusion zone dimensions and cooling rates in part scale laser powder bed fusion. Additive Manufacturing **46**, 102222 (2021) https://doi.org/10.1016/j.addma.2021.102222

[42] Weaver, J.S., Heigel, J.C., Lane, B.M.: Laser spot size and scaling laws for laser beam additive manufacturing. Journal of Manufacturing Processes **73**, 26–39 (2022) https://doi.org/10.1016/j.jmapro.2021.10.053

[43] Ye, J., Khairallah, S.A., Rubenchik, A.M., Crumb, M.F., Guss, G., Belak, J., Matthews, M.J.: Energy coupling mechanisms and scaling behavior associated with laser powder bed fusion additive manufacturing. Advanced Engineering Materials **21**(1), 1900185 (2019) https://doi.org/10.1002/adem.201900185

[44] Rubenchik, A.M., King, W.E., Wu, S.S.: Scaling laws for the additive manufacturing. Journal of Materials Processing Technology **257**, 234–243 (2018) https://doi.org/10.1016/j.jmatprotec.2018.02.034

[45] Fabbro, R.: Scaling laws for the laser welding process in keyhole mode. Journal of Materials Processing Technology **264**, 346–351 (2019) https://doi.org/10.1016/j.jmatprotec.2018.09.027

[46] Sharma, S., Krishna, K.V.M., Joshi, S.S., Radhakrishnan, M., Palaniappan, S., Dussa, S., Banerjee, R., Dahotre, N.B.: Laser based additive manufacturing of tungsten: Multi-scale thermo-kinetic and thermo-mechanical computational model and experiments. Acta Materialia **259** (2023) https://doi.org/10.1016/j.actamat.2023.119244

[47] Haynes, W.M.: Handbook of Chemistry and Physics, 95th edn. CRC, New York (2015)

[48] Tang, C., Le, K.Q., Wong, C.H.: Physics of humping formation in laser powder bed fusion. International Journal of Heat and Mass Transfer **149**, 119172 (2020) https://doi.org/10.1016/j.ijheatmasstransfer.

2019.119172

[49] Cagran, C.: Thermal conductivity and thermal diffusivity of liquid copper. Technical report, Technische Universitat Graz (2000)

[50] Assael, M.J., Kalyva, A.E., Antoniadis, K.D., Banish, R.M., Egry, I., Wu, J., Kaschnitz, E., Wakeham, W.A.: Reference data for the density and viscosity of liquid copper and liquid tin. Journal of Physical and Chemical Reference Data **39**, 33105 (2010) https://doi.org/10.1063/1.3467496

[51] Dai, D., Gu, D.: Tailoring surface quality through mass and momentum transfer modeling using a volume of fluid method in selective laser melting of tic/alsi10mg powder. International Journal of Machine Tools and Manufacture **88**, 95–107 (2015) https://doi.org/10.1016/j.ijmachtools.2014.09.010